Journal of Physics and Chemistry of Solids 144 (2020) 109502

Contents lists available at ScienceDirect

Journal of Physics and Chemistry of Solids

journal homepage: http://www.elsevier.com/locate/jpcs

Influence of nucleating agent addition on the textural and photo-Fenton properties of Fe(III)/SiO_2 catalysts

Julien G. Mahy [a,*], Sophie Hermans [a], Rémi G. Tilkin [b,c], Stéphanie D. Lambert [b]

[a] Institute of Condensed Matter and Nanosciences (IMCN), Université catholique de Louvain, Place Louis Pasteur 1, B-1348, Louvain-la-Neuve, Belgium
[b] Department of Chemical Engineering – Nanomaterials, Catalysis, Electrochemistry, B6a, University of Liège, B-4000, Liège, Belgium
[c] Centre Interfacultaire des Biomatériaux (CEIB), University of Liège, Allée du Six Août 11, B-4000, Liège, Belgium

ARTICLE INFO

Keywords:
Sol–gel synthesis
Fe/SiO_2 xerogels
Modified silicon alkoxide
Co-gelation method
Photo-Fenton process

ABSTRACT

Two Fe-based/SiO_2 catalysts have been prepared by a sol–gel method, with or without co-gelation with a modified silicon alkoxide, 3-(2-aminoethylamino)propyltrimethoxysilane (EDAS). The aim was to compare these two materials and to study the influence of EDAS on the catalyst texture and photo-Fenton activity. Physico-chemical characterization showed that when EDAS was used, the iron was located inside the silica nanoparticles and was partially arranged in iron oxide clusters. As EDAS is a nucleating agent for silica, the reaction time was shorter in its presence, leading to larger silica nanoparticles. Studies of their behavior in aqueous media showed that the catalyst without EDAS released iron, whereas the catalyst with EDAS did not. This iron release influenced the photo-Fenton activities of the catalysts. *p*-Nitrophenol was degraded more rapidly with the catalyst without EDAS due to the greater availability of iron. Finally, both Fe/SiO_2 catalysts displayed stable catalytic activity for 72 h of operation.

1. Introduction

Controlling the pollutant concentrations in our rivers and lakes is a topic of steadily increasing importance. Severe pollution can have fatal consequences for human health (e.g., breathing or cardiovascular problems, cancer, and neurobehavioral disorders) and the environment (e.g., serious damage to fauna and flora) [1]. Wastewater treatment plants are able to remove the majority of pollutants from our wastewaters. However, some substances that are present in small quantities cannot be degraded by these conventional plants and accumulate in the environment. These so-called micropollutants mostly result from domestic and industrial uses of pharmaceutical preparations, cosmetic and hygiene products, and pesticides. Therefore, it is important to direct our research efforts towards the development of a ternary treatment step for water exiting the clarifier, whereby these micropollutants can be degraded. Among the technologies that could be applied to degrade such compounds, advanced oxidative processes (AOPs) represent promising candidates. These techniques involve redox reactions for the degradation of organic substrates, such as chemical pollutants or even microorganisms [2,3]. They are effective at atmospheric pressure and ambient temperatures. Examples of AOPs are ozonolysis, titania-based photocatalysis, and the (photo-)Fenton process [2,3].

The photo-Fenton process involves the use of H_2O_2, Fe(III), and light irradiation to induce the production of hydroxyl radicals ($HO^{\bullet}$) [4,5]. This process is driven by the Fenton reaction, which is the catalyzed production of $HO^{\bullet}$ from H_2O_2 using iron ions (Equation (1)) [4,5].

$$Fe^{2+} + H_2O_2 \rightarrow Fe^{3+} + OH^- + HO^{\bullet} \quad (1)$$

In this case, Fe(II) is required to induce the Fenton reaction [4]. In a photo-Fenton process, Fe(III) can be used by virtue of its partial reduction to Fe(II) under light irradiation (Equation (2)) [4].

$$Fe^{3+}(L)_n + h\nu \rightarrow Fe^{2+}(L)_{n-1} + L_{ox}^{\bullet} \quad (2)$$

where L is a ligand, $L_{ox}^{\bullet}$ is an oxidized ligand, h is the Planck constant (6.63×10^{-34} J s), and ν is the light frequency (Hz). The ligand is regenerated after reaction of the oxidized ligand with organic molecules.

Various photo-Fenton systems have been developed [4,6–9]. Usually, the Fe(III) catalyst is an iron salt that is dissolved in the reaction medium [6–9]. Heterogenization of the iron catalyst on a support introduces the advantage of its easy recovery for reuse. In this case, the support needs to allow a high dispersion of the iron species and to have a high specific surface area to increase the water–catalyst contact. There have been several reports of the use of zeolites, titania, alumina, or silica

* Corresponding author.
E-mail address: julien.mahy@uclouvain.be (J.G. Mahy).

https://doi.org/10.1016/j.jpcs.2020.109502
Received 13 November 2019; Received in revised form 6 April 2020; Accepted 8 April 2020
Available online 14 April 2020

as supports for Fe(III) species [10–13]. Among these supports, silica seems to be a good candidate as it is inexpensive, porous, non-toxic, and easily produced by different synthesis methods [14]. Among these methods, sol–gel chemistry allows the production of highly porous silica materials under mild synthesis conditions [15]. In recent years, an innovative co-gelation method has been developed for producing mono- or bimetallic supported catalysts in a single step [16–21]. This co-gelation method permits synthesis of the support (SiO_2) as well as dispersion of the metallic precursor of the active species at the same time, owing to the use of a modified silicon alkoxide that disperses the metallic species [20,22]. This modified silicon alkoxide is also a nucleating agent for silica particles [23]. Hence, the catalysts obtained exhibit a very specific structure [20,22,24,25].

This work focuses on the development of Fe(III)/SiO_2 materials and understanding the influence of co-gelation synthesis parameters on their textural properties and photo-Fenton activities in order to degrade environmentally harmful substances in water. To this end, two iron catalysts supported on silica were produced by a sol–gel process, with and without a modified silicon alkoxide, 3-(2-aminoethylamino)propyltrimethoxysilane (EDAS), as a nucleating agent. The main advantages of this preparation method are the low reaction temperature (<100 °C), the very good dispersion of metallic species achieved in one step, and the high resistance to sintering of the metallic or oxide nanoparticles located in the silica matrix [26]. The corresponding pure silica materials were also synthesized. The photo-Fenton efficacies of the materials were tested under UV/visible light for the degradation of *p*-nitrophenol (PNP), an archetypal pollutant derived from pesticides. The catalytic stabilities of the materials were also assessed over 72 h of operation.

2. Materials and methods

2.1. Catalyst synthesis

The starting reagents and solvents for the synthesis were 3-(2-aminoethylamino)propyltrimethoxysilane (EDAS, Merck, 97%), absolute ethanol (EtOH, Merck, >99%), tetraethoxysilane (TEOS, Sigma-Aldrich, 98%), Fe(III) acetylacetonate ($Fe(acac)_3$, Sigma-Aldrich, 97%), ammonium hydroxide solution (28% NH_3 in H_2O, Sigma-Aldrich, ≥99.99%), and distilled water.

The amounts of reagents used to prepare all of the samples are given in Table 1. Two iron xerogel catalyst samples (with the same iron content) and two pure SiO_2 samples were prepared with and without the modified alkoxide (EDAS). The samples prepared with EDAS are denoted with "–E", those with iron with "Fe", and those with only silica with "SiO_2". The synthesis protocol was similar to previously published methods [27,28]. The samples were prepared in EtOH, with $Fe(acac)_3$ (or without for pure silica), TEOS, EDAS (or without), and 0.54 M NH_3 aqueous solution. The hydrolysis ratio and the dilution ratio were set at 5 and 10, respectively [27,28].

For gelation and aging, the sample vessel was sealed and heated to 80 °C for 72 h [27,28]. The gel time of each sample was determined visually: if the sample no longer flowed when the glass bottle was tilted to 45°, it was considered gelled [27,28]. Thereafter, the gels were dried under vacuum at 80 °C. The pressure was slowly decreased to 100 Pa after 120 h. The samples were then heated to 150 °C for 72 h at 100 Pa [27,28].

The samples were calcined at 450 °C, attained at a rate of 120 °C h^{-1}, under flowing air for 8 h [27,28]. They were then heated to 550 °C at a rate of 120 °C h^{-1} under flowing air for 4 h [27,28]. These two calcination steps ensured maximum removal of the solvent and unreacted molecules [29].

2.2. Characterization of the materials

Nitrogen adsorption–desorption isotherms were measured with a Micromeritics ASAP 2420 analyzer. Mercury porosimetry measurements were performed between 0.01 and 200 MPa using two Thermo Scientific Pascal 140 and 240 devices. The nitrogen adsorption–desorption isotherms were used to calculate the specific surface area by the Brunauer–Emmett–Teller (BET) method, S_{BET}; the specific mesopore surface area determined by the Broekhoff–de Boer theory, S_{BdB}; the specific mesopore volume determined by the Broekhoff–de Boer theory, $V_{cum<7.5nm}$; the specific micropore volume calculated by the Dubinin–Radushkevich theory, V_{DR}; and the specific liquid volume adsorbed at the saturation pressure of nitrogen, V_P [27,28,30]. The specific macropore volume, V_{Hg}, was estimated through mercury porosimetry measurements [31]. A combination of nitrogen adsorption–desorption isotherms and mercury porosimetry was used to calculate the pore size distribution [23,27,28].

The amount of iron in the samples was determined by inductively coupled plasma–atomic emission spectroscopy (ICP–AES), using an ICAP 6500 Thermo Scientific device. Solutions for analysis were prepared as follows [27]: (i) Na_2O_2 (2 g), NaOH (1 g), and sample (0.1 g) were mixed in a vitreous carbon crucible; (ii) the mixture was heated beyond the melting point (up to 950 °C); (iii) after cooling and solidification, the mixture was digested in 65% HNO_3 (30 mL); (iv) the solution was then transferred to a calibrated flask and diluted to 500 mL with deionized water [27].

The size of the silica nanoparticles was measured by transmission electron microscopy (TEM) using a Phillips CM 100 microscope (accelerating voltage 200 kV).

X-ray diffraction (XRD) patterns were recorded with a Bruker D8 Twin-Twin powder diffractometer employing Cu-K_α radiation.

X-ray photoelectron spectroscopy measurements were carried out on an SSI X probe spectrometer (model SSI 100, Surface Science Laboratories) equipped with a monochromated Al-K_α radiation source (1486 eV).

Mössbauer spectra were obtained on a constant acceleration spectrometer at 295 K with a cobalt-57 source calibrated with α-iron foil.

The amounts of iron released into aqueous media over 35 days were also measured for the two iron-doped samples. A weighed amount of calcined xerogel (0.55 g/L, 10^{-4} M in iron) was immersed in ultrapure water under stirring, and then the iron contents of withdrawn aliquots were measured by ICP-AES after removing the xerogel by filtration. The first sampling (day 0) was taken after 10 min of stirring, then samples were taken each day for the first seven days (days 1–7) and thereafter once every seven days (days 14, 21, 28, and 35).

Table 1
Synthesis operating variables.

Sample	Ethanol (mmol)	TEOS (mmol)	EDAS (mmol)	Water (mmol)	Fe $(acac)_3$ (mmol)	EDAS/ TEOS	Gel time (min)	Theoretical iron loading (wt%)	Actual iron loading[a] (wt %)
SiO_2-E	2570	249	8.37	1274	0	0.033	30	0	0
Fe1-E	2570	249	8.37	1274	2.79	0.033	20	1.0	1.0
SiO_2	2570	257	0	1284	0	–	170	0	0
Fe1	2570	257	0	1284	2.79	–	50	1.0	0.98

[a] Measured by ICP-AES.

2.3. Photo-Fenton experiments

The photo-Fenton activities of the samples were evaluated by following the degradation of *p*-nitrophenol (PNP) for 24 h under different conditions, in triplicate, as detailed in a previous report [27]. The experimental set-up is shown in Ref. [27]. The residual concentration of PNP was measured by UV/Vis spectrophotometry (GENESYS 10S UV–Vis, Thermo Scientific) at 318 nm. Four different conditions were tested: with or without light, and with or without H_2O_2. In each flask, the initial concentrations of iron, PNP, and H_2O_2 (if present) were 10^{-4} M (0.55 g/L), 10^{-4} M, and 10^{-3} M, respectively. For the pure silica sample, the same mass of xerogel was used as for the iron-doped samples (0.55 g/L). The illumination source was a halogen lamp with a continuous spectrum between 300 and 800 nm (300 W, 220 V). The temperature was maintained at 20 °C.

To evaluate the stability of the iron-doped catalysts for the photo-Fenton reaction, the xerogels were recovered by centrifugation (10000 rpm for 1 h) and then dried at 100 °C for 24 h. A new photocatalytic experiment as described above was then performed with each used catalyst. This recovery procedure was performed twice for a total of 72 h of operation for each catalyst. Nitrogen adsorption–desorption isotherms of the used catalysts were also measured to assess whether the porous structure had changed after several catalytic experiments.

To confirm complete mineralization of the pollutant during the photo-Fenton experiments, total organic carbon (TOC) measurements were performed using a Hach DRB200 reactor and a Total Organic Carbon Direct Method Test N Tube™ Reagent Set [28,32]. The TOC was determined by first sparging the sample under slightly acidic conditions to remove the inorganic carbon [28,32]. In an external vial, the organic carbon contained in the sample was digested by persulfate and acid to form carbon dioxide. During digestion, the carbon dioxide diffuses into a pH indicator reagent in an inner ampoule [28,32]. The adsorption of carbon dioxide onto the indicator forms carbonic acid, which influences the pH of the indicator solution, thus changing its color. The degree of color change is related to the original amount of carbon present in the sample and can be evaluated by measuring the absorbance at 430 nm, for which we used a Hach DR 2800 spectrophotometer [28,32].

3. Results

3.1. Macroscopic aspects and composition

The iron contents measured in the samples are listed in Table 2. For both doped samples, the theoretical and actual iron percentages are similar (i.e., ca. 1 wt%).

The pure silica samples are white powders, characteristic of silica materials. In contrast, the iron-doped samples are yellow. The Fe1 sample (Fig. 1a) has a more intense color than Fe1-E (Fig. 1b), which is pale-yellow. This yellow color is associated with the Fe(III) oxidation state [33] and its intensity is related to the location of iron in the samples. If the iron were located at the surface, the color would be more intense than for a sample with the iron located within the silica matrix.

The presence of iron was studied by XRD (see the Supplementary Materials, Fig. S1); no peak associated with iron species was observed due to the very low iron content. X-ray photoelectron spectroscopy (XPS) was also performed, and again no peak associated with iron species could be detected (see Supplementary Materials, Fig. S2). This is due to the sol–gel method, which leads to localization but high dispersion of the small amount of iron within the bulk of the material rather than on its surface.

The iron species were further studied by Mössbauer measurements, as presented in Fig. 2. For Fe1, only one signal is observed, in the form of an asymmetrical broad doublet. For Fe1-E, a similar doublet is observed (red contribution), along with an additional broad singlet (blue contribution).

3.2. Catalyst morphology

Fig. 3 shows TEM images of the iron-doped samples. Nanoparticle sizes are given in Table 2. For Fe1-E, two types of nanoparticles can be observed (Fig. 3a): small nanoparticles (around 1 nm diameter) inside larger nanoparticles (i.e., ca. 20–25 nm). The small nanoparticles correspond to iron species, which are dispersed in larger silica particles. For Fe1 (Fig. 3b), only silica nanoparticles are observed, of size around 17 nm. For the two pure silica samples, the silica particles are seen to be smaller than those of SiO_2-E (8 *vs.* 35 nm).

Fig. 4 shows the nitrogen adsorption–desorption isotherms for the four samples. Two different isotherm shapes can be observed. For SiO_2,

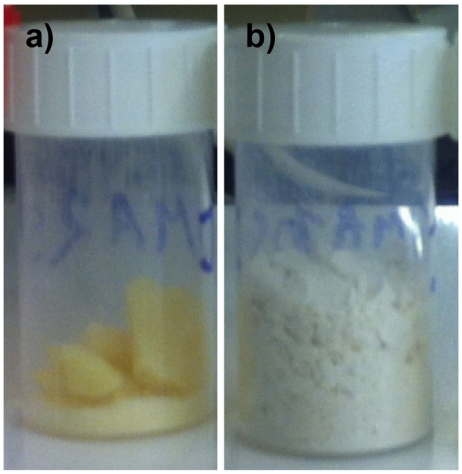

Fig. 1. Visual appearance of (a) Fe1 and (b) Fe1-E samples.

Table 2
Textural properties of xerogel catalyst samples.

Sample	d_{TEM} (nm)	S_{BET} (m^2 g^{-1}) ±5	S_{BdB} (m^2 g^{-1}) ±5	V_P (cm^3 g^{-1}) ±0.1	V_{DR} (cm^3 g^{-1}) ±0.01	$V_{cum<7.5nm}$ (cm^3 g^{-1}) ±0.01	V_{Hg} (cm^3 g^{-1}) ±0.1	P_t (MPa)	k (nm $MPa^{0.25}$)	V_T (cm^3 g^{-1}) ±0.1	S_{CYC} (m^2 g^{-1}) ±5
SiO_2-E	35 ± 6	215	80	0.8	0.09	0.05	2.8	21	158	2.9	-[a]
Fe1-E	23 ± 5	230	145	0.4	0.09	0.04	3.2	32	111	3.4	225
SiO_2	8.4 ± 1	615	120	1.6	0.26	0.45	2.6	-[b]	-[b]	3.3	-[a]
Fe1	17 ± 3	315	240	1.3	0.14	0.14	1.6	98	48	1.9	295

[a] Not measured.

[b] Not applicable; d_{TEM}: mean diameter of silica particles measured by TEM; S_{BET}: specific surface area determined by the BET method; S_{BdB}: specific mesopore surface area determined by the Broekhoff–de Boer theory; V_p: specific liquid volume adsorbed at the saturation pressure of nitrogen; V_{DR}: specific micropore volume determined by the Dubinin–Raduskevitch theory; $V_{cum<7.5nm}$: cumulative volume pores of diameter between 2 and 7.5 nm determined by Broekhoff-de-Boer theory; V_{Hg}: specific pore volume measured by mercury porosimetry; P_t: pressure of change of mechanism during mercury porosimetry (change from collapse to intrusion); k: buckling model constant; V_T: pore volume obtained by addition of V_{DR}, $V_{cum<7.5nm}$, and V_{Hg}; S_{CYC}: specific surface area determined by the BET method after 72 h of photocatalytic experiments.

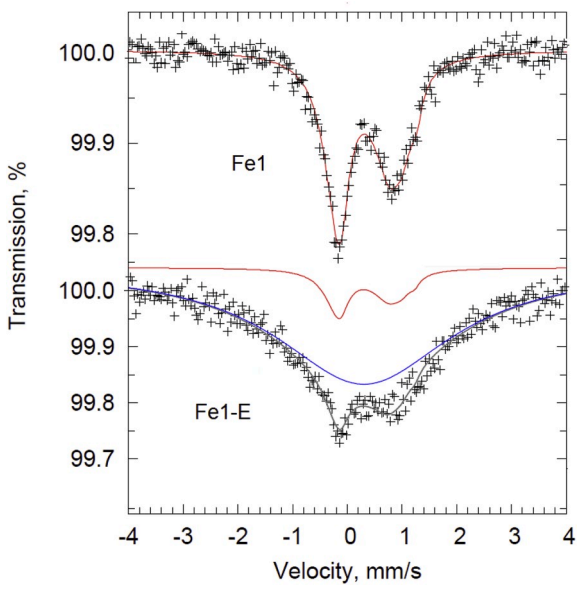

Fig. 2. Transmission iron-57 Mössbauer spectra of Fe1 and Fe1-E samples.

SiO_2-E, and Fe1, the isotherms correspond to a mixture of types I and II according to the Brunauer–Deming–Deming–Teller (BDDT) classification [30], characterized by a sharp increase at low relative pressure followed by a plateau (type I, microporous solid), and at high pressure the adsorbed volume increases rapidly as for type II isotherms (macroporous solid). Only Fe1-E displays hysteresis at high pressures, corresponding to mesopores. For the Fe1-E sample, the isotherm is a mixture of types I and IV according to the BDDT classification [30], characterized by a sharp increase at low relative pressure followed by a plateau (type I, microporous solid) and a broad hysteresis (type IV, mesoporous solid). The specific surface areas, S_{BET}, range from 215 to 615 m^2/g for the four samples (Table 2).

Mercury porosimetry curves are presented in Fig. 5. Under increasing mercury pressure, samples SiO_2-E, Fe1-E, and Fe1 display two successive behaviors [27,34]: (i) at low pressure, the samples collapse under the isostatic pressure; (ii) above the transition pressure (P_t), mercury enters their pores. P_t can be discerned in the pressurization curve by a change of slope [27]. Two models are used to describe these two phenomena and to calculate the pore size distribution [27]. The collapse of larger pores below P_t is described by Pirard's model [31], and mercury intrusion above P_t is described by Washburn's equation [31]. The SiO_2 sample (Fig. 5, empty circles) displays only one behavior, corresponding to a collapse under the isostatic pressure; no change of slope is observed.

The combination of nitrogen adsorption–desorption isotherm and mercury porosimetry allows the pore size distribution of the samples to be calculated [23], which is represented in Fig. 6 for Fe1 as an example (the other results are presented in the Supplementary Materials, Figs. S3–S5). These distributions were calculated by different methods applied in their respective validity domains: (i) Brunauer's method (micropores); (ii) Broekhoff-de Boer's method (mesopores smaller than 7.5 nm); and (iii) Pirard's and Washburn's models (pores larger than 7.5 nm) [23,27]. The associated volumes are given in Table 2 for all of the samples. All samples are characterized by a steep volume increase at around 0.7–0.8 nm due to the micropores, followed by a broad distribution in the meso- and macropore range. Therefore, they contained the three types of pores (micro-, meso-, and macropores).

3.3. Behavior in water

The two Fe/SiO_2 xerogels were stirred in water for 35 days, and the amounts of iron released into the aqueous medium were measured. The results are presented in Table 3. The amount of iron leached was lower than the detection limit for Fe1-E. For Fe1, iron was detected immediately when the sample was placed in the water (day 0). Thereafter, the leached amount increased in the first 2 days, and then remained constant. Iron is therefore more available in the Fe1 sample.

3.4. Photo-Fenton activity

All of the catalysts were tested with or without H_2O_2 for the production of $HO^{\bullet}$ radicals to degrade the model organic molecule. Only in those experiments in which a combination of light and H_2O_2 was deployed was PNP degraded, as presented in Fig. 7. Without any catalyst, 64% of PNP was degraded after 24 h. When pure silica was used, the degradations were slightly lower at 55% and 61% with the SiO_2-E and SiO_2 samples, respectively. As regards the iron catalysts, degradations were enhanced to 76% and 99% for the Fe1-E and Fe1 samples, respectively. Table 4 provides a comparison of the PNP degradation percentages after 24 h of illumination as determined by UV/Vis spectrophotometry and TOC measurements. Both measurements are similar, so the observed degradation of PNP observed by UV/Vis spectrophotometry corresponds to its mineralization during the photocatalytic experiments. UV/Vis spectrophotometry was then used for the majority of the experiments as it is easier and quicker to apply.

The stability of the activity was also assessed by three successive photocatalytic experiments with the iron-doped samples. The mean PNP degradation rates for Fe1-E and Fe1 were evaluated as 74 ± 2% and 96 ± 3%, respectively, showing stability of the catalyst activity (Fig. 7a).

The UV/Vis spectra of PNP after 24 h of illumination for the different samples are shown in Fig. 7b, along with the initial PNP spectrum. The PNP degradation percentages (Fig. 7a) were calculated according to the decrease of the peak at 318 nm.

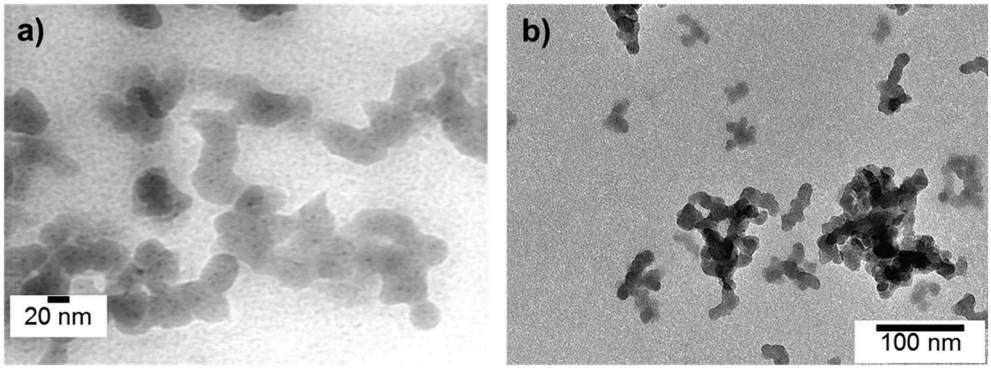

Fig. 3. TEM images of (a) Fe1-E and (b) Fe1 samples.

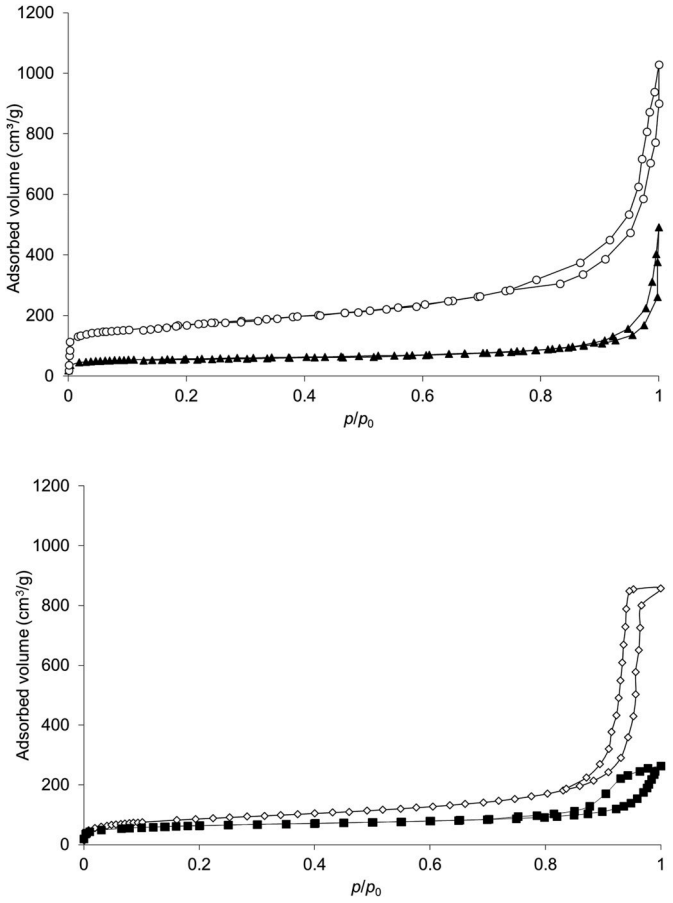

Fig. 4. Nitrogen adsorption–desorption isotherms for (▲) SiO_2-E, (○) SiO_2, (■) Fe1-E, and (◊) Fe1 samples.

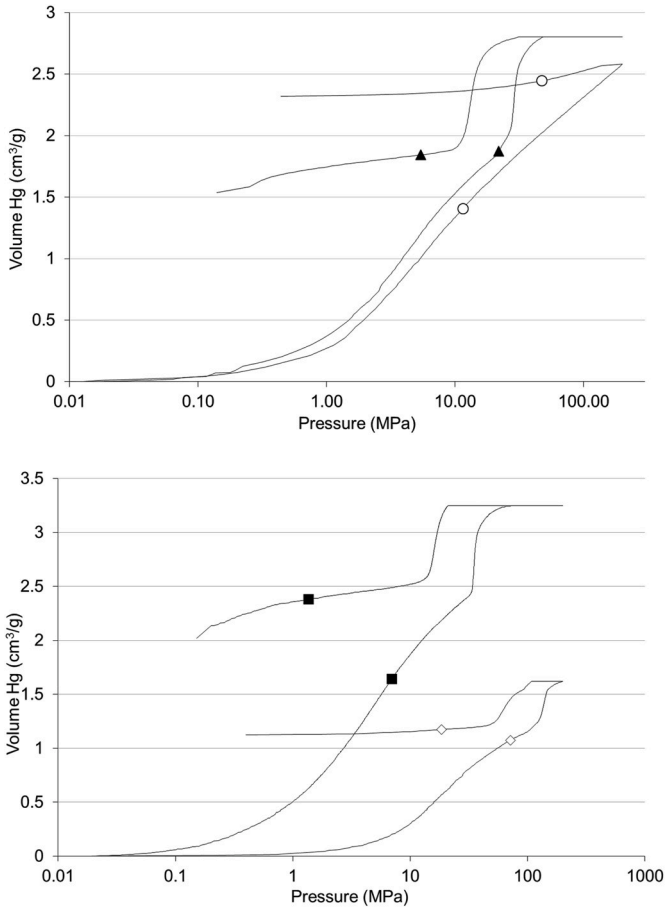

Fig. 5. Mercury porosimetry curves for (▲) SiO_2-E, (○) SiO_2, (■) Fe1-E, and (◊) Fe1 samples.

4. Discussion

4.1. Iron species

ICP measurements confirmed the presence of iron in the samples, but not the oxidation state.

The yellow color of the iron-doped powders is characteristic of the Fe^{3+} state [33]. The difference in color intensity of the two iron/SiO_2 catalysts can be ascribed to the use of the modified silicon alkoxide (EDAS), which can complex iron ions during synthesis and encapsulate the iron in the silica matrix during the co-gelation process. The Fe1-E sample was paler than Fe1 (Fig. 1). For Fe1, Fe^{3+} species are present randomly in or at the surface of the silica.

Mössbauer spectra (Fig. 2) give more information about the iron species present. For Fe1-E, the spectrum is composed of two contributions that correspond to (i) iron oxide nanoparticles (blue curve), also visualized as the small nanoparticles observed by TEM (Fig. 3), and (ii) Fe^{3+} ions (red curve) dispersed in the silica matrix [27]. For Fe1, only the contribution of Fe^{3+} ions (red curve) dispersed in the silica matrix is obtained, consistent with the TEM images, as no small iron-based nanoparticles were observed in the silica matrix in this case. The difference in the nature of the iron species types arises from the use of EDAS, which bears an ethylenediamine group (Fig. 8) that is able to complex the Fe^{3+} ions. When EDAS is used, the Fe^{3+} ions can regroup inside the silica matrix due to their complexation, producing iron oxide clusters [20,35]. When no EDAS is used in the synthesis, the iron content is distributed throughout the silica, both at the surface and in the matrix.

The complexing effect of EDAS was evident from iron release experiments (Table 3). When the two iron-doped samples were stirred in water, Fe1 presumably released the iron located on its surface, whereas

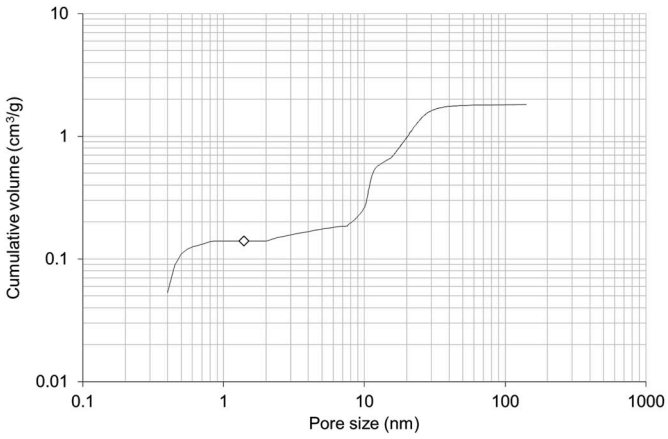

Fig. 6. Pore size distribution for the Fe1 sample.

Fe1-E retained the iron that was anchored inside its silica matrix. The iron release in turn influences the photo-Fenton activities of the catalysts (Fig. 7, see Section 4.3).

4.2. Catalyst textures

From the N_2 isotherms and Hg porosimetry results (Figs. 4 and 5), two main factors affecting the texture of the xerogels can be identified: the use of EDAS and the iron content.

It has been shown previously [23] that the modified alkoxide EDAS is

Table 3
Levels of released iron in aqueous media for the two Fe/SiO_2 samples.

Time (day)	Fe1	Fe1-E
	iron concentration (mol/L)	iron concentration (mol/L)
0	7.5×10^{-7}	< detection limit
1	1.1×10^{-6}	< detection limit
2	2.8×10^{-6}	< detection limit
3	1.1×10^{-6}	< detection limit
4	1.5×10^{-6}	< detection limit
7	1.6×10^{-6}	< detection limit
14	1.8×10^{-6}	< detection limit
21	2.5×10^{-6}	< detection limit
28	2.3×10^{-6}	< detection limit
35	2.9×10^{-6}	< detection limit

Detection limit of ICP-AES = 3.6×10^{-8} mol/L.

a nucleating agent for silica particles. When the amount of EDAS is increased in a TEOS/EDAS mixture, the number of silica particles and the gel time decrease. Indeed, in this study, the gel time (Table 1) decreased when EDAS was used. For example, the gel times were 30 and 170 min for the SiO_2-E and SiO_2 samples, respectively. When no EDAS was used (i.e., pure SiO_2), the reaction time was very long; the reactants slowly reacted homogeneously in the solution and the particles were very small (Table 2) as there was no preferential nucleation point. The specific surface area was quite large for the SiO_2 sample (Table 2) as the particles were very small. In Hg porosimetry curves, the position of the inflection point (the transition pressure, P_t) is also related to the silica particle size [23]. An inflection point displaced to higher pressure corresponds to smaller silica particles. The size measured by TEM (Table 2) is consistent with the Hg porosimetry results. The SiO_2-E sample had the largest silica nanoparticle size and the lowest transition pressure P_t during mercury porosimetry. The pure SiO_2 sample was composed of small nanoparticles, which resulted in no inflection point.

Concerning the effect of iron content, this parameter is influenced by the ligand used in the iron salt, namely acetylacetonate [27]. This ligand has basic character, and it catalyzes hydrolysis and condensation reactions [36] during the sol–gel synthesis. Hence, the gel time decreases when iron is added, as can be observed in Table 1. The Fe1-E sample had a shorter gel time as it contained both iron salt and EDAS.

4.3. Catalyst activity

Catalytic experiments conducted in the dark showed that the catalysts did not adsorb the PNP, so the observed decreases in PNP concentration were entirely due to a degradation process.

In Fig. 7a (first blue bar), it can be seen that when PNP was in contact with H_2O_2 under illumination without any catalyst, the degree of degradation was 64%. H_2O_2 undergoes direct photolysis under light of wavelength $\lambda < 360$ nm [9,37,38] and produces $HO^\bullet$ radicals according to Equation (3).

$$H_2O_2 + h\nu \rightarrow 2\ HO^\bullet \quad (3)$$

In this case, these radicals degrade the PNP. When pure silica samples are used, the degradation rate decreases slightly to 55% and 61% for SiO_2-E and SiO_2, respectively. It is known that silica has no photocatalytic activity [27]; no increase in degradation rate is thus logical. The decrease of activity seen here may stem from a shadow effect of the silica, reducing the efficiency of Equation (3). The putative shadow effect is more pronounced for SiO_2-E as its particles are larger than those

Table 4
Total organic carbon (TOC) measurements after photocatalytic experiments (24 h of illumination).

Photocatalytic experiments after 24 h of illumination with H_2O_2	Remaining organic carbon (%) ±1	PNP degradation (%) ±3	Remaining PNP (%) ±3
With H_2O_2 only	34	64	36
With SiO_2-E	49	55	45
With Fe1-E	27	76	24
With SiO_2	37	61	39
With Fe1	0	99	1

The remaining organic carbon was calculated from the TOC measurement before and after the catalytic experiment = $\frac{TOC_{final}}{TOC_{initial}} \times 100$

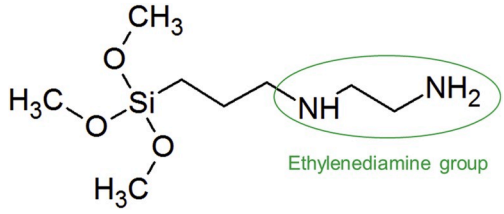

Fig. 8. Molecular structure of EDAS, highlighting the ethylenediamine group (drawn with ACD/ChemSketch).

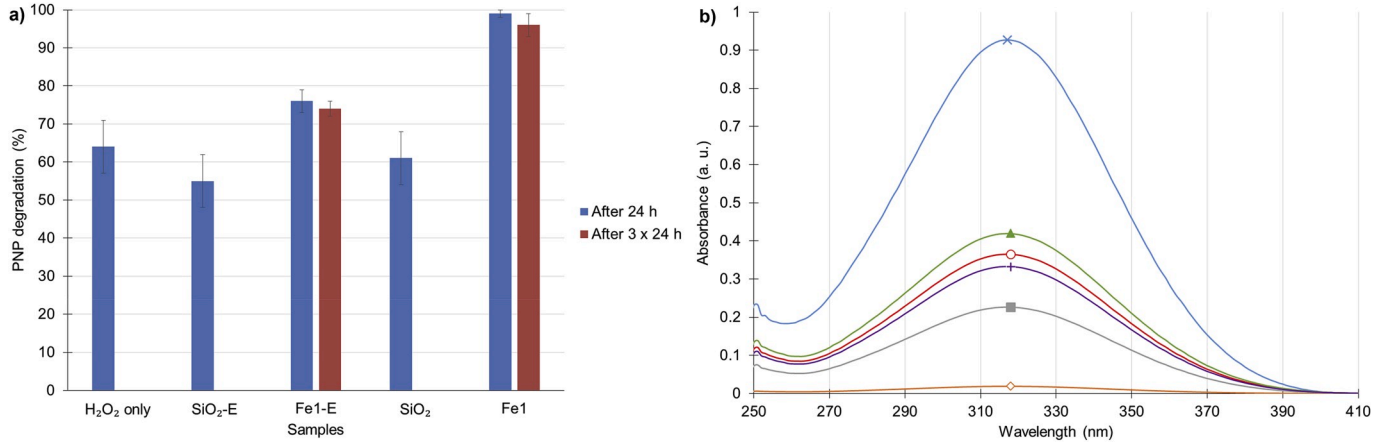

Figure 7. (a) *p*-Nitrophenol (PNP) degradation with H_2O_2 (10^{-4} M) under UV/Vis light (300–800 nm) after 24 h of illumination (blue) and after 3 × 24 h for the iron-doped samples (red). The catalyst concentration was 1 g/L. (b) Evolution of the UV/Vis spectrum of PNP during the photocatalytic experiment (with H_2O_2) (x) at initial concentration of 10^{-4} M, (+) after 24 h of illumination with only H_2O_2, (▲) after 24 h of illumination with SiO_2-E, (○) after 24 h of illumination with SiO_2, (■) after 24 h of illumination with Fe1-E, and (◇) after 24 h of illumination with Fe1. (For an interpretation of the references to color in the text, the reader is referred to the web version of this article.)

of SiO_2. When the particles are very small with respect to the wavelength of light (30 nm *vs.* 300 nm), the scattering can be described as Rayleigh scattering, which scales as R^4, where R is the radius of the particles [39]. If the concentration remains constant, then the number of particles per volume scales by R^{-3}, that is to say, the smaller the particles, the more particles per volume [39]. Therefore, the scattering power per volume scales with R: the larger the particles, the greater the light scattering [39], which reduces the transmission of light towards H_2O_2.

To assess the shadow effect of silica, similar photocatalytic experiments were performed with different amounts of SiO_2-E (0.55, 1, 2, and 5 g/L). The degrees of PNP degradation after 24 h of illumination were 55, 34, 21, and 16%, respectively. This confirms that silica decreases light diffusion in the solution, reducing the production of radicals from H_2O_2.

When iron-based catalysts are used, the PNP degradation is improved. Fe^{3+} ions can produce Fe^{2+} and radicals according to Equation (2) [4].

The radicals produced increase the degradation of organic pollutants and the Fe^{2+} ions produced catalyze the decomposition of H_2O_2 into $HO^\bullet$ according to the Fenton reaction [4], leading to an increase in the number of radical species. The equations involved in radical production are as follows [8,40–42]:

$$Fe^{2+} + H_2O_2 \rightarrow Fe^{3+} + OH^- + HO^\bullet \quad (4)$$

$$Fe^{3+} + H_2O_2 \rightarrow Fe^{2+} + HO_2^\bullet + H^+ \quad (5)$$

$$HO^\bullet + H_2O_2 \rightarrow HO_2^\bullet + H_2O \quad (6)$$

$$HO^\bullet + Fe^{2+} \rightarrow Fe^{3+} + OH^- \quad (7)$$

$$Fe^{3+} + HO_2^\bullet \rightarrow Fe^{2+} + O_2 + H^+ \quad (8)$$

$$Fe^{2+} + HO_2^\bullet + H^+ \rightarrow Fe^{3+} + H_2O_2 \quad (9)$$

$$HO_2^\bullet + HO_2^\bullet \rightarrow H_2O_2 + O_2 \quad (10)$$

$$HO_2^\bullet + H_2O_2 \rightarrow HO^\bullet + H_2O + O_2 \quad (11)$$

The radicals produced can attack and degrade the organic pollutant (PNP), converting it into CO_2 and H_2O [8,40–42] as follows.

$$HO^\bullet/HO_2^\bullet/O_2 + PNP \rightarrow CO_2 + H_2O \quad (12)$$

The mineralization was demonstrated by TOC measurements (Table 4), and proved to be complete for the Fe1 sample.

The activity of Fe1-E is lower than that of the Fe1 sample, which can only be attributed to the EDAS introduced in the synthesis of Fe1-E. As described above, the iron in Fe1-E is encapsulated within the silica matrix and is less available when the sample is in contact with water (Table 3). Moreover, a part of the iron forms iron oxide clusters and is probably less available for photo-Fenton reactions. In contrast, the Fe1 sample shows iron release in water (Table 3), making it directly available for photo-Fenton reactions.

Recycled batches of both iron catalysts displayed stable activity after three experiments (72 h), showing that silica acts as a reservoir of iron, releasing the ions over time.

5. Conclusions

Two Fe (1 wt%)/SiO_2 catalysts have been prepared by a sol–gel process with or without the use of the modified silicon alkoxide 3-(2-aminoethylamino)propyltrimethoxysilane (EDAS). The goals of this work were to study the influence of EDAS on the texture and photocatalytic properties of the catalysts. The two corresponding pure silica materials were also synthesized as references.

EDAS is a nucleating agent for silica particles and complexes iron ions during the sol–gel synthesis. These two properties impart different textural and morphological characteristics. With EDAS, larger silica particles were obtained, with iron encapsulated within the silica matrix. Moreover, two iron species were observed: dispersed Fe^{3+} ions and iron oxide clusters. Without EDAS, smaller silica nanoparticles were produced after a longer gelation time. In this case, only Fe^{3+} ions dispersed in silica were observed.

The iron-doped sample without EDAS showed immediate iron release when placed in contact with water, whereas the sample with EDAS showed no detectable leaching.

The photo-Fenton activities of the two iron-doped samples can be directly linked to their specific morphologies. The iron-doped sample without EDAS displayed the best PNP degradation rate due to the direct availability of iron. Nevertheless, the sample with EDAS showed an increase of PNP degradation compared to a blank experiment without catalyst, while limiting the iron leaching in water. Both samples maintained their photoefficiency after three consecutive experiments, that is to say, 72 h of operation.

Declaration of competing interest

The authors declare that they have no conflicts of interest.

CRediT authorship contribution statement

Julien G. Mahy: Conceptualization, Methodology, Investigation, Writing - original draft. **Sophie Hermans:** Investigation. **Rémi G. Tilkin:** Investigation. **Stéphanie D. Lambert:** Supervision, Funding acquisition, Project administration.

Acknowledgements

S.H. and S.D.L. are grateful to F.R.S.-F.N.R.S for their Senior Research Associate positions. R.G.T. benefits from the Fund for Scientific Research (FNRS) under a Fund for Research Training in Industry and Agriculture (FRIA) grant. The authors acknowledge the Ministère de la Région Wallonne Direction Générale des Technologies, de la Recherche et de l'Energie (DGO6), the Fonds de Bay, and the Fonds de Recherche Fondamentale et Collective for financial support. J.G.M. and S.H. also thank Innoviris Brussels for financial support through the Bridge project – COLORES.

Appendix A. Supplementary data

Supplementary data to this article can be found online at https://doi.org/10.1016/j.jpcs.2020.109502.

References

[1] M.A. Khan, A.M. Ghouri, Environmental Pollution: its effects on life and its remedies, J. Arts Sci. Commer 2 (2011) 276–285. https://ssrn.com/abstract=1981242.
[2] D.B. Miklos, C. Remy, M. Jekel, K.G. Linden, J.E. Drewes, U. Hübner, Evaluation of advanced oxidation processes for water and wastewater treatment – a critical review, Water Res. 139 (2018) 118–131, https://doi.org/10.1016/j.watres.2018.03.042.
[3] M. Sillanpää, M.C. Ncibi, A. Matilainen, Advanced oxidation processes for the removal of natural organic matter from drinking water sources: a comprehensive review, J. Environ. Manag. 208 (2018) 56–76, https://doi.org/10.1016/j.jenvman.2017.12.009.
[4] J.J. Pignatello, E. Oliveros, A. MacKay, Advanced oxidation processes for organic contaminant destruction based on the Fenton reaction and related chemistry, Crit. Rev. Environ. Sci. Technol. 36 (2006) 1–84, https://doi.org/10.1080/10643380500326564.
[5] N.B. Parilti, D. Akten, Application of Box-Wilson experimental design method for the solar photocatalytic degradation of textile dyestuff with Fe(III)/H_2O_2/solar UV process, Desalination 260 (2010) 193–198, https://doi.org/10.1016/j.desal.2010.04.040.
[6] F.H. Borba, J. Leichtweis, F. Bueno, L. Pellenz, J.J. Inticher, D. Seibert, Pollutant removal and acute toxicity assessment (*Artemia salina*) of landfill leachate treated by photo-Fenton process mediated by oxalic acid, J. Water Process Eng. 28 (2019) 159–168, https://doi.org/10.1016/j.jwpe.2019.01.017.
[7] S. Giannakis, M. Voumard, S. Rtimi, C. Pulgarin, Bacterial disinfection by the photo-Fenton process: extracellular oxidation or intracellular photo-catalysis?

Appl. Catal. B Environ. 227 (2018) 285–295, https://doi.org/10.1016/j.apcatb.2018.01.044.
[8] M. Li, Z. Qiang, C. Pulgarin, J. Kiwi, Accelerated methylene blue (MB) degradation by Fenton reagent exposed to UV or VUV/UV light in an innovative micro photoreactor, Appl. Catal. B Environ. 187 (2016) 83–89, https://doi.org/10.1016/j.apcatb.2016.01.014.
[9] L. Xu, L. Meng, X. Zhang, X. Mei, X. Guo, W. Li, et al., Promoting Fe^{3+}/Fe^{2+} cycling under visible light by synergistic interactions between P25 and small amount of Fenton reagents, J. Hazard Mater. 379 (2019) 120795, https://doi.org/10.1016/j.jhazmat.2019.120795.
[10] J.G. Mahy, F. Deschamps, V. Collard, C. Jérôme, J. Bartlett, S.D. Lambert, et al., Acid acting as redispersing agent to form stable colloids from photoactive crystalline aqueous sol–gel TiO_2 powder, J. Sol. Gel Sci. Technol. 87 (2018) 568–583, https://doi.org/10.1007/s10971-018-4751-6.
[11] R. Cui, S. Ma, J. Wang, S. Sun, NO oxidation over Fe-based catalysts supported on montmorillonite K10, γ-alumina and ZSM-5 with gas-phase H_2O_2, Chemosphere 234 (2019) 302–309, https://doi.org/10.1016/j.chemosphere.2019.06.029.
[12] I. Fechete, E. Gautron, E. Dumitriu, D. Lutic, P. Caullet, H. Kessler, Studies on the acidity and the stability of Fe^{3+} ions in the framework of (Si,Fe)-MCM-22 zeolite. Selective *para*-xylene production by toluene disproportionation, Rev. Roum. Chem. 53 (2008) 49–54.
[13] J.A. Melero, G. Calleja, F. Martínez, R. Molina, K. Lázár, Crystallization mechanism of Fe-MFI from wetness impregnated Fe_2O_3-SiO_2 amorphous xerogels: role of iron species in Fenton-like processes, Microporous Mesoporous Mater. 74 (2004) 11–21, https://doi.org/10.1016/j.micromeso.2004.06.002.
[14] G. Busca, Catalytic materials based on silica and alumina: structural features and generation of surface acidity, Prog. Mater. Sci. 104 (2019) 215–249, https://doi.org/10.1016/j.pmatsci.2019.04.003.
[15] C. Alié, A. Benhaddou, R. Pirard, A.J. Lecloux, J.P. Pirard, Textural properties of low-density xerogels, J. Non-Cryst. Solids 270 (2000) 77–90, https://doi.org/10.1016/S0022-3093(00)00076-4.
[16] S.L. Pirard, J.G. Mahy, J.-P. Pirard, B. Heinrichs, L. Raskinet, S.D. Lambert, Development by the sol-gel process of highly dispersed Ni-Cu/SiO_2 xerogel catalysts for selective 1,2-dichloroethane hydrodechlorination into ethylene, Microporous Mesoporous Mater. 209 (2015) 197–207, https://doi.org/10.1016/j.micromeso.2014.08.015.
[17] J.G. Mahy, V. Claude, L. Sacco, S.D. Lambert, Ethylene polymerization and hydrodechlorination of 1,2-dichloroethane mediated by nickel(II) covalently anchored to silica xerogels, J. Sol. Gel Sci. Technol. 81 (2017) 59–68, https://doi.org/10.1007/s10971-016-4272-0.
[18] S. Lambert, F. Ferauche, A. Brasseur, J.P. Pirard, B. Heinrichs, Pd-Ag/SiO_2 and Pd-Cu/SiO_2 cogelled xerogel catalysts for selective hydrodechlorination of 1,2-dichloroethane into ethylene, Catal. Today 100 (2005) 283–289, https://doi.org/10.1016/j.cattod.2004.08.015.
[19] B. Breitscheidel, J. Zieder, U. Schubert, Metal complexes in inorganic matrices. 7. Nanometer-sized, uniform metal particles in a silica matrix by sol-gel processing of metal complexes, Chem. Mater. 3 (1991) 559–566, https://doi.org/10.1021/cm00015a037.
[20] U. Schubert, Heterobimetallic sol–gel precursors and intermediates, J. Sol. Gel Sci. Technol. 79 (2016) 249–261, https://doi.org/10.1007/s10971-015-3920-0.
[21] S.C. Warren, M.R. Perkins, A.M. Adams, M. Kamperman, A.A. Burns, H. Arora, et al., A silica sol-gel design strategy for nanostructured metallic materials, Nat. Mater. 11 (2012) 460–467, https://doi.org/10.1038/nmat3274.
[22] S. Lambert, K.Y. Tran, G. Arrachart, F. Noville, C. Henrist, C. Bied, et al., Tailor-made morphologies for Pd/SiO_2 catalysts through sol-gel process with various silylated ligands, Microporous Mesoporous Mater. 115 (2008) 609–617, https://doi.org/10.1016/j.micromeso.2008.03.003.
[23] S. Lambert, C. Alié, J.P. Pirard, B. Heinrichs, Study of textural properties and nucleation phenomenon in Pd/SiO_2, Ag/SiO_2 and Cu/SiO_2 cogelled xerogel catalysts, J. Non-Cryst. Solids 342 (2004) 70–81, https://doi.org/10.1016/j.jnoncrysol.2004.06.005.
[24] C. Diaz, M.L. Valenzuela, D. Garrido, A. Pedro, Sol-gel incorporation of organometallic compounds into silica: useful precursors to metallic nanostructured materials, J. Chil. Chem. Soc. 2 (2012) 1155–1162, https://doi.org/10.4067/S0717-97072012000200021.
[25] A. Safavi, A. Banazadeh, F. Sedaghati, Synthesis of palladium nanoparticles on organically modified silica: application to design of a solid-state electrochemiluminescence sensor for highly sensitive determination of imipramine, Anal. Chim. Acta 796 (2013) 115–121, https://doi.org/10.1016/j.aca.2013.08.015.
[26] S. Lambert, C. Cellier, P. Grange, J.P. Pirard, B. Heinrichs, Synthesis of Pd/SiO_2, Ag/SiO_2, and Cu/SiO_2 cogelled xerogel catalysts: study of metal dispersion and catalytic activity, J. Catal. 221 (2004) 335–346, https://doi.org/10.1016/j.jcat.2003.07.014.
[27] J.G. Mahy, L. Tasseroul, A. Zubiaur, J. Geens, M. Brisbois, M. Herlitschke, et al., Highly dispersed iron xerogel catalysts for *p*-nitrophenol degradation by photo-Fenton effects, Microporous Mesoporous Mater. 197 (2014) 164–173, https://doi.org/10.1016/j.micromeso.2014.06.009.
[28] J.G. Mahy, L. Tasseroul, O. Tromme, B. Lavigne, S.D. Lambert, Hydrodechlorination and complete degradation of chlorinated compounds with the coupled action of Pd/SiO_2 and Fe/SiO_2 catalysts: towards industrial catalyst synthesis conditions, J. Environ. Chem. Eng. 7 (2019) 103014, https://doi.org/10.1016/j.jece.2019.103014.
[29] B. Heinrichs, L. Rebbouh, J.W. Geus, S. Lambert, H.C.L. Abbenhuis, F. Grandjean, et al., Iron(III) species dispersed in porous silica through sol-gel chemistry, J. Non-Cryst. Solids 354 (2008) 665–672, https://doi.org/10.1016/j.jnoncrysol.2007.07.071.
[30] A.J. Lecloux, Texture of catalysts, Catal. Sci. Technol. 2 (1981) 171.
[31] R. Pirard, B. Heinrichs, O. Van Cantfort, J.P. Pirard, Mercury porosimetry applied to low density xerogels; relation between structure and mechanical properties, J. Sol. Gel Sci. Technol. 13 (1998) 335–339, https://doi.org/10.1023/A:1008676211157.
[32] C.M. Malengreaux, G.M.-L. Léonard, S.L. Pirard, I. Cimieri, S.D. Lambert, J. R. Bartlett, et al., How to modify the photocatalytic activity of TiO_2 thin films through their roughness by using additives. A relation between kinetics, morphology and synthesis, Chem. Eng. J. 243 (2014) 537–548, https://doi.org/10.1016/j.cej.2013.11.031.
[33] M. Clugston, R. Flemming, Advanced Chemistry, Oxford University Press, 2000.
[34] C. Alié, N. Tcherkassova, F. Ferauche, S. Lambert, B. Heinrichs, R. Pirard, et al., Multigram scale synthesis and characterization of low-density silica xerogels, J. Non-Cryst. Solids 352 (2006) 2763–2771, https://doi.org/10.1016/j.jnoncrysol.2006.03.054.
[35] M. Guglielmi, A. Martucci, Sol-gel nanocomposites, in: L. Klein (Ed.), Handb. Sol-Gel Sci. Technol., Springer Nature, 2018, pp. 3041–3063.
[36] C.J. Brinker, G.W. Scherer, Sol-gel Science: the Physics and Chemistry of Sol-Gel Processing, Academic Press, 2013.
[37] S.R. Pouran, A.R.A. Aziz, W. Mohd, A. Wan, Review on the main advances in photo-Fenton oxidation system for recalcitrant wastewaters, J. Ind. Eng. Chem. 21 (2015) 53–69, https://doi.org/10.1016/j.jiec.2014.05.005.
[38] T.M. El-Morsi, M.M. Emara, H.M.H. Abd, E. Bary, A.S. Abd-El-Aziz, K.J. Friesen, Homogeneous degradation of 1,2,9,10-tetrachlorodecane in aqueous solutions using hydrogen peroxide, iron and UV light, Chemosphere 47 (2002) 343–348.
[39] J.G. Mahy, S.D. Lambert, R.G. Tilkin, D. Poelman, C. Wolfs, F. Devred, et al., Ambient temperature ZrO_2-doped TiO_2 crystalline photocatalysts: highly efficient powders and films for water depollution, Mater. Today: Energy 13 (2019) 312–322, https://doi.org/10.1016/j.mtener.2019.06.010.
[40] T. Guo, K. Wang, G. Zhang, X. Wu, A novel α-Fe_2O_3@g-C_3N_4 catalyst: synthesis derived from Fe-based MOF and its superior photo-Fenton performance, Appl. Surf. Sci. 469 (2019) 331–339, https://doi.org/10.1016/j.apsusc.2018.10.183.
[41] J. Li, C. Xiao, K. Wang, Y. Li, G. Zhang, Enhanced generation of reactive oxygen species under visible light irradiation by adjusting the exposed facet of $FeWO_4$ nanosheets to activate oxalic acid for organic pollutant removal and Cr(VI) reduction, Environ. Sci. Technol. 53 (2019) 11023–11030, https://doi.org/10.1021/acs.est.9b00641.
[42] M. Li, D. Wen, Z. Qiang, J. Kiwi, VUV/UV light inducing accelerated phenol degradation with a low electric input, RSC Adv. 7 (2017) 7640–7647, https://doi.org/10.1039/c6ra26043h.